



## Springtime transition in lower thermospheric atomic oxygen

Gordon G. Shepherd, Jacek Stegman, Patrick Espy J., Charles Mclandress, Gérard Thuillier, R. H. Wiens

### ► To cite this version:

Gordon G. Shepherd, Jacek Stegman, Patrick Espy J., Charles Mclandress, Gérard Thuillier, et al.. Springtime transition in lower thermospheric atomic oxygen. *Journal of Geophysical Research Space Physics*, 1999, 104 (A1), pp.213-223. <10.1029/98JA02831>. <insu-01627448>

**HAL Id: insu-01627448**

**<https://insu.hal.science/insu-01627448v1>**

Submitted on 22 Dec 2020

**HAL** is a multi-disciplinary open access archive for the deposit and dissemination of scientific research documents, whether they are published or not. The documents may come from teaching and research institutions in France or abroad, or from public or private research centers.

L'archive ouverte pluridisciplinaire **HAL**, est destinée au dépôt et à la diffusion de documents scientifiques de niveau recherche, publiés ou non, émanant des établissements d'enseignement et de recherche français ou étrangers, des laboratoires publics ou privés.



HAL Authorization

# Springtime transition in lower thermospheric atomic oxygen

G. G. Shepherd,<sup>1</sup> J. Stegman,<sup>2</sup> P. Espy,<sup>3,4</sup> C. McLandress,<sup>1</sup> G. Thuillier,<sup>5</sup> and R.H. Wiens<sup>1</sup>

**Abstract.** Observations from three optical ground stations and the wind imaging interferometer on the upper atmosphere research satellite have been combined to describe a "springtime transition" in atomic oxygen. At each station the transition is characterized by a rapid 2-day rise in the night-time oxygen airglow emission rate by a factor of between 2 and 3, with a subsequent decrease by a factor of about 10 in the same period of time. This latter state of extremely weak oxygen airglow indicates a depletion of atomic oxygen that persists for many days. The characteristic signature is similar at both mid-latitude and high-latitude stations and is also observed in the hydroxyl airglow, except that immediately following the enhancement, the hydroxyl emission rate does not fall below the value it had before the event. Airglow rotational temperatures behave coherently with the emission rate. WINDII data show that the airglow emission rate perturbation is a planetary scale feature associated with strong vertical motions and that the event may be associated with the winter-to-summer zonal wind reversal. Data from the northern springtimes of 1992 and 1993 are reported upon in detail, with additional data from 1995 to confirm the persistence of the phenomenon.

## 1. Introduction

The wind imaging interferometer (WINDII) on the upper atmosphere research satellite (UARS) measures upper atmospheric winds and emission rates from airglow-excited species [Shepherd *et al.*, 1993]. During the validation of WINDII [Gault *et al.*, 1996; Thuillier *et al.*, 1996], ground-based instruments were operated at Bear Lake, Utah (42°N, 212°E), and the Observatoire de Haute-Provence (41°N, 6°E) in southern France. In early April, 1992, the night-time observations at Bear Lake showed an increase in the emission rate of the O<sub>2</sub> atmospheric (0,1) band, by a factor of about 2 in just 2 days, followed immediately by a dramatic drop of more than a factor of 10 in the days following. The emission rate remained low for about 5 days, before making a partial recovery and then returning to lower values again. This behavior closely resembled an effect previously discovered at Stockholm (60°N, 20°E) [Stegman *et al.*, 1992]. Although the Stockholm winter is normally marked by enhancements in airglow emission rate, followed by rapid decreases to the original level, the end of winter is marked by a similar enhancement with one distinct difference. During the winter the emission rate before and after the enhancement is the same, but for the springtime event the emission rate following the enhancement is much lower than that before and lower than that observed at any time during the winter. The behavior at Stockholm is slightly different from that at Bear Lake in that the emission rate may remain low for several weeks, not returning to

normal values again before the onset of summer high-latitude daylight. The winter events are associated with stratospheric warmings, while the focus in this paper is directed solely toward this springtime feature. Here we show data for four springtime periods, but J. Stegman (manuscript in preparation, 1998) presents in detail the behavior from 1985 to 1997, clearly showing that the basic characteristics do repeat year after year. A similar effect was found for the Observatoire de Haute-Provence.

Since the nighttime oxygen airglow is produced by atomic oxygen recombining according to  $O + O + M \rightarrow O_2^* + M$ , the reduction in airglow emission rate indicates a decrease in the concentration of atomic oxygen in the airglow layer, thus signaling a "depletion" in atomic oxygen concentration. Since there cannot be any significant change in the production rate of atomic oxygen through  $O_2 + h\nu \rightarrow O + O$  in such a short period of time, the change must result from dynamical effects. WINDII data are therefore presented for the northern spring of 1992, in order to examine the global scale dynamical behavior in winds and emission rates.

The Bear Lake Observatory (BLO) is operated by Utah State University for optical measurements. The instruments normally operated there were supplemented by others during the two WINDII validation years, 1991–1992 and 1992–1993. Results on other aspects of this collaboration have been described elsewhere [Wiens *et al.*, 1995]. The Meteorological Institute of Stockholm University (MISU) has operated an airglow observatory (J. Stegman, manuscript in preparation, 1998) for about 13 years, involving detailed spectral and photometric observations of the oxygen airglow and related emissions. The Observatoire de Haute-Provence (OHP) has a long-standing record of airglow observations and it supported the validation of WINDII wind measurements with the Michelson interferometer for coordinated auroral Doppler observations (MICADO) instrument [Thuillier *et al.*, 1996]. In this study we first present data from the WINDII validation periods March 20 to May 9 of the years 1992 and 1993, when data from all three sites were available, and then we briefly compare with data from two ground sites for 1995. The ground-based observations are thus provided by three stations, two of which are at almost the same latitude, BLO and OHP, and 2 of which are at almost the same longitude, OHP and MISU.

<sup>1</sup>Centre for Research in Earth and Space Science, York University, Toronto, Ontario, Canada.

<sup>2</sup>Arrhenius Laboratory, Stockholm University, Stockholm.

<sup>3</sup>Space Dynamics Laboratory, Utah State University, Logan.

<sup>4</sup>Department of Physical Sciences, Embry-Riddle Aeronautical University, Daytona Beach, Florida.

<sup>5</sup>Service d'Aéronomie, Verrières-le-Buisson, France.

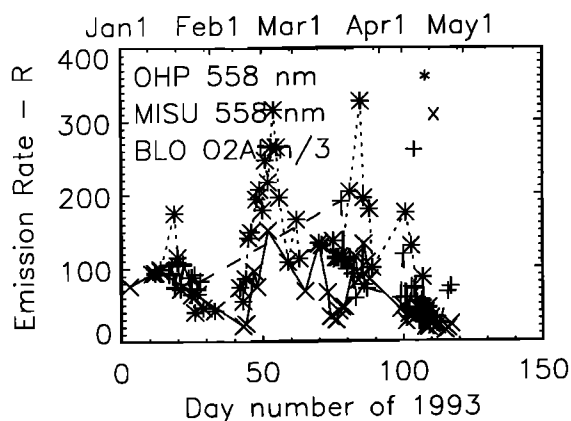


**Figure 1.** Vertically integrated (zenithal) emission rates for nighttime oxygen airglow for January-May, 1993, as observed at Observatoire de Haute-Provence (OHP), Meteorological Institute of Stockholm University (MISU), and Bear Lake Observatory (BLO) of Utah State University.

The UARS orbit has an inclination of  $57^\circ$ , and WINDII looks to the antisunward side of the spacecraft at  $45^\circ$  and  $135^\circ$  from the velocity vector. The consequence is that at any given time, WINDII views latitudes ranging from  $42^\circ$  in one hemisphere to  $72^\circ$  in the opposite hemisphere. During about 36 days the Sun moves through  $180^\circ$  with respect to the orbit plane, so that the spacecraft must be rotated through  $180^\circ$  to keep the Sun on the same side of the satellite. Since WINDII was viewing southward during the study periods, there were no observations north of  $42^\circ$ , thus eliminating the possibility of Stockholm overflights. However, this is compensated for to some extent by excellent longitudinal coverage at  $42^\circ\text{N}$ , the location of BLO and OHP, which is the northward turning point of the WINDII fields of view. Within this latitudinal range, WINDII provides global coverage for each day that the atomic oxygen (OI) 558-nm emission was observed. For a given day all the data for the ascending crossings of a specific latitude band have approximately the same local time, while the descending crossings of the same latitude band also have nearly constant but different local times. Thus all emission rate maps shown in this

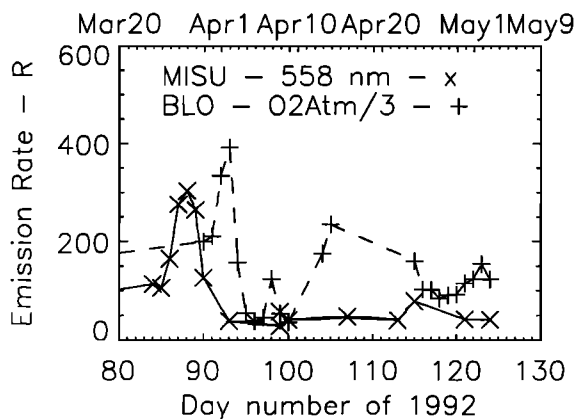


**Figure 2.** Vertically integrated (zenithal) emission rate for oxygen airglow for the period March 20 to May 3, 1992, for BLO ( $\text{O}_2$  atmospheric band) and MISU atomic oxygen (OI) 557.7-nm emission.

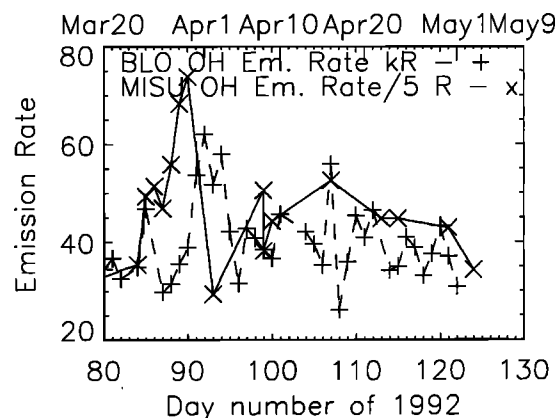


**Figure 3.** Hydroxyl zenithal emission rates observed at BLO and MISU during the spring of 1992. The BLO values are for the entire Meinel system and are in Kilorayleigh, while the MISU measurements are for the (8,3) band divided by 5, in rayleigh (R).

paper will be for either the ascending or descending crossings. Because the local time is nearly constant for a given latitude, the longitudinal variations observed are not due to the migrating solar tide but are true planetary scale features. The migrating tide makes some contribution to the observed perturbation but with the same values for all longitudes at that latitude. Day-by-day coverage for the OI 557.7-nm emission is not possible for 1992, since WINDII then was cycled through different emissions day by day and the nighttime green line emission, from near 97-km altitude, was observed only every third day. WINDII data from the  $\text{O}_2$  atmospheric band emission near 94 km and the Meinel band emission from the hydroxyl radical near 87 km are available, but their presentation is beyond the scope of this paper.

## 2. Ground-based Observations

In Figure 1 we show the vertically integrated (zenithal) emission rate in rayleigh (R) for the nighttime oxygen emissions observed at all three sites (BLO, MISU, and OHP) for the winter through spring period of 1993. There is one data point for each

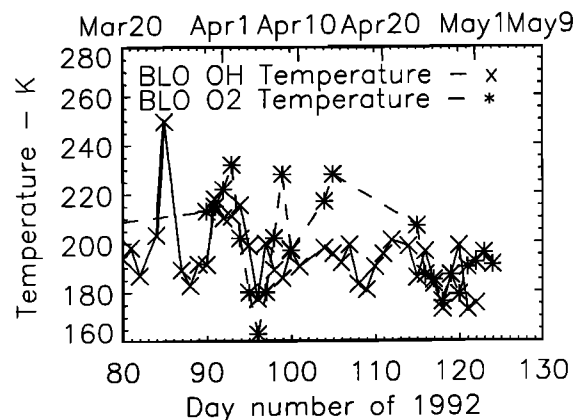


**Figure 4.** Rotational temperature measurements at BLO for an OH Meinel band and the  $\text{O}_2$  atmospheric (0,1) band during the spring of 1992.

night of observations, corresponding to the average for that night, providing to some extent an averaging over the tidal variations during the night. There is a minor enhancement in mid-January, a major one near the end of February, and a significant one near the end of March. The first of these is seen clearly in the OHP data, with a maximum to minimum ratio of more than 4, while the data here are sparse for BLO and MISU. The enhancement at the end of February is seen clearly by OHP (a maximum-to-minimum ratio of 6) and at MISU with a ratio of 5; no BLO data were taken during this time period. The enhancement at the end of March is seen at all sites, at roughly the same time at OHP and MISU (which are at the same longitude) and earlier at BLO. Following this enhancement, all sites show a decline in emission rate over a period of about 20 days, such that by the end of April the emission rates at all three sites have reached consistently low values, with about 15 R of 557.7-nm emission at MISU. This is a factor of 10 lower than the values seen at the winter peaks. As stated earlier, it is these very low springtime values of emission rate, indicating a large-scale depletion of atomic oxygen, that are the focus of this paper.

We examine the springtime behavior in more detail in the 1992 data of Figure 2, which shows the BLO and MISU emission rates for the period March 20 to May 3. Specifically, this is the 557.7-nm emission at MISU and the  $O_2$  atmospheric band emission observed by the Mesopause Oxygen Rotational Temperature Imager (MORTI) [Wiens *et al.*, 1991] at BLO. Toward the end of March there are sharply defined emission rate peaks at both stations, occurring 5 days earlier at MISU than at BLO. However, the most remarkable aspect is the sharp drop in emission rate after the peak, reaching about 30 R for the 557.7-nm emission at MISU (from a peak value of 300 R) and 90 R for the (0,1)  $O_2$  atmospheric band at BLO from a peak of 1200 R. To summarize, the emission peaks are a factor of 2-3 higher than the emission rates preceding the peak, but the emission rates after the peak are lower than the peak by about a factor of 10. This is similar to the situation for 1993 shown in Figure 1, except that for 1992 the depletions occur much more rapidly following the enhancements.

With durations of about 5 days the enhancements look roughly similar at BLO and MISU, apart from the BLO time delay of 5 days, but the behavior patterns after the respective peaks are very different. For the 60° latitude of MISU the emission rate remains at a very low level, lower than that for all of the preceding winter (not shown here), until summer sunlit conditions take over. For the 42° latitude of BLO the values indicate oxygen depletion for about 5 days, followed by a recovery (unfortunately largely obscured by cloud), then followed by a return to a moderately depleted condition. OHP data were not available for this year.

In Figure 3 we show the hydroxyl emission rates measured at MISU and BLO for the spring of 1992; hydroxyl emission occurs at about 87 km, about 10 km below the altitude of the OI 557.7-nm emission and 7 km below that of the  $O_2$  atmospheric band emission. There is considerable similarity between the hydroxyl (Figure 3) and atomic oxygen green line (Figure 2) airglow patterns. The hydroxyl peaks are broader than the oxygen peaks and even appear double, but the centers of these double peaks do coincide with the centers of the oxygen peaks for the same stations. The 5-day delay for BLO as compared to MISU is as clearly seen in the hydroxyl data as in the oxygen data. The difference as compared to atomic oxygen is that for both MISU and BLO there is no depletion of hydroxyl emission following the peaks but an immediate return to prepeak levels. Since atomic oxygen is also involved in the production of the hydroxyl

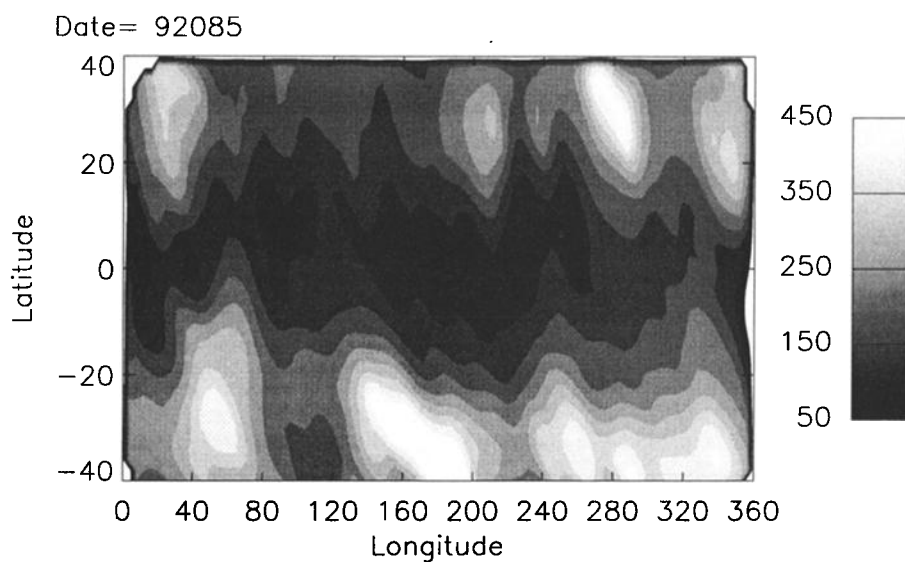
emission, the coherence with the green line emission shows that the enhancement of atomic oxygen is common to both altitude levels but that the depletion of atomic oxygen does not persist at an altitude of 87 km. Temperature data are shown in Figure 4, with hydroxyl and  $O_2$  atmospheric band temperatures both obtained at BLO. By comparing with Figures 2 and 3 it is apparent that there is a high degree of coherence between the temperature patterns and the emissions from which the temperatures are derived. While the hydroxyl temperature clearly shows an enhancement of about 30 K, it returns immediately afterwards to the prepeak temperature values, as was the case for the emission. However, the  $O_2$  atmospheric band temperature drops from about 230 K at the peak to a remarkably low value of 163 K on April 5 during the time of highly depleted atomic oxygen.

### 3. Satellite Emission Rate Observations

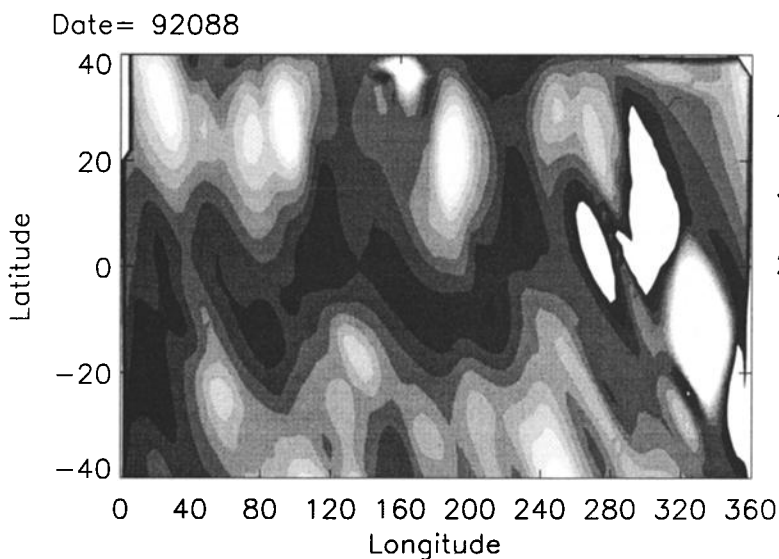
WINDII normally observed nighttime atomic oxygen green line airglow every 3 days in 1992, with an  $O(^1D)$  red line day once a week as explained in section 1. Thus we present atomic oxygen  $O(^1S)$  557.7-nm emission rate maps for the following nights in 1992: March 25, 28, and 31 and April 4, 7, and 14 (data were not available for the scheduled day of April 11). In Figure 5a we show the March 25 data in a form that may be directly compared with the ground-based observations, namely, vertically integrated emission rate for the atomic oxygen green line emission, plotted on a latitude longitude map for the latitude range -40° - 40°. For this night, which is prior to both the Stockholm and Bear Lake enhancements, we see a clearly defined equatorial minimum, characteristic of the equatorial airglow in the postmidnight hours, as described by Shepherd *et al.* [1995]. At 30°N the local time is about 0240 LT, and at 30°S it is 2330 LT, while at the equator it is near 2400 LT. The minimum oscillates slightly about the equator. At higher latitudes there are prominent planetary scale structures, particularly in the southern hemisphere where they resemble wavenumber 3.

Figure 5b shows the same situation for March 28, 1992, the day of the MISU peak. The mid-latitude planetary scale patterns persist but are now more prominent in the northern hemisphere than in the southern, the opposite of what was observed 3 days earlier. The tropical emission has brightened and become a sinusoidal (wavenumber-3) emission valley, with a width of about 15° and an amplitude of about 20° in latitude. The emission rates at 40°N are weak, with no obvious connection to the enhancement occurring at the same time at Stockholm.

In Figure 5c for March 31 the emission rates are still low at Stockholm longitudes, but there are strong localized regions near 260° and 340° longitude. These are east of BLO (at 212°) but March 31 is still prior to the BLO peak. It appears as though these enhancements traveled westward, consistent with Figure 5b, and passed over Bear Lake 2 days later. In Figure 5d for April 4 all signs of zonal continuity in the equatorial minimum have vanished, with bright equatorial features near the longitudes of 50° and 180° and deep depletions near longitudes of 240° and 300°. The latter depletion extends to both north and south latitudes, and near 35°N latitude it spreads longitudinally, extending westward past Bear Lake, which agrees well with the observation from Figure 2 that the BLO depletion is just under way on April 4. Thus the satellite view not only confirms the ground-based observation but shows that this depletion is of planetary scale, extending from at least 40°S to 40°N. The depletion observed during the same period at Stockholm may be



**Figure 5a.** Vertically integrated (zenithal) emission rate for the  $O(^1S)$  558-nm airglow measured by the wind imaging interferometer (WINDII) for March 25, 1992. The bar indicates the emission rate in rayleigh.



**Figure 5b.** Vertically integrated (zenithal) emission rates for the  $O(^1S)$  558-nm airglow measured by WINDII for March 28, 1992.

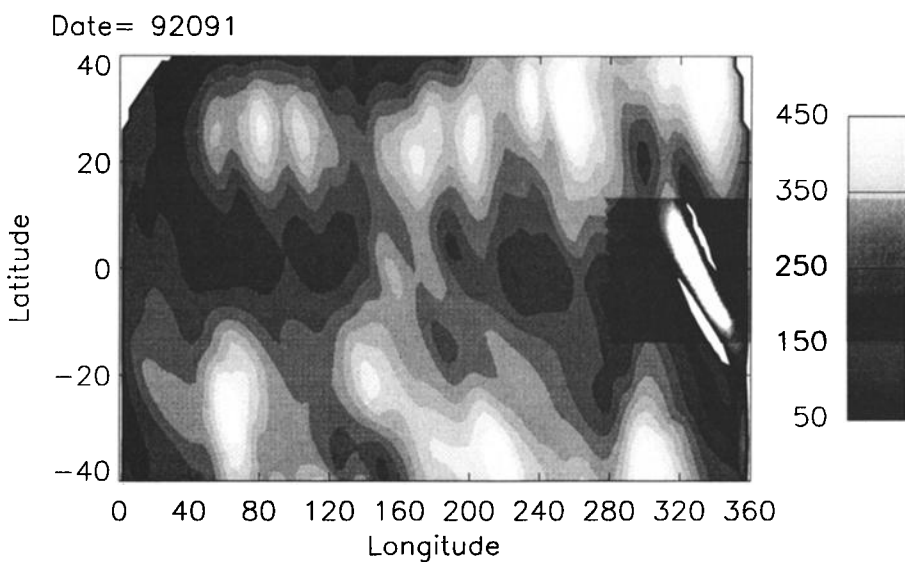


**Figure 5c.** Vertically integrated (zenithal) emission rates for the  $O(^1S)$  558-nm airglow measured by WINDII for March 31, 1992.

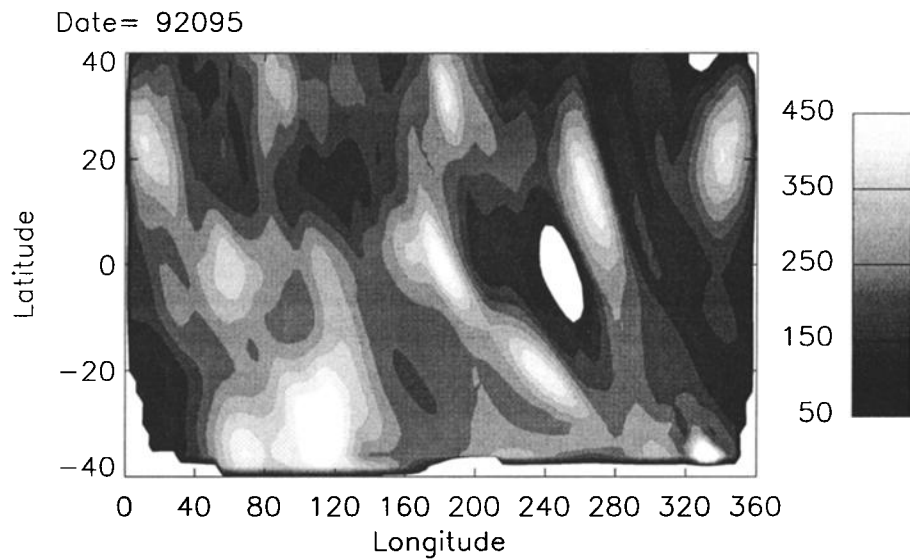


**Figure 5d.** Vertically integrated (zenithal) emission rates for the O(<sup>1</sup>S) 558-nm airglow measured by WINDII for April 4, 1992.

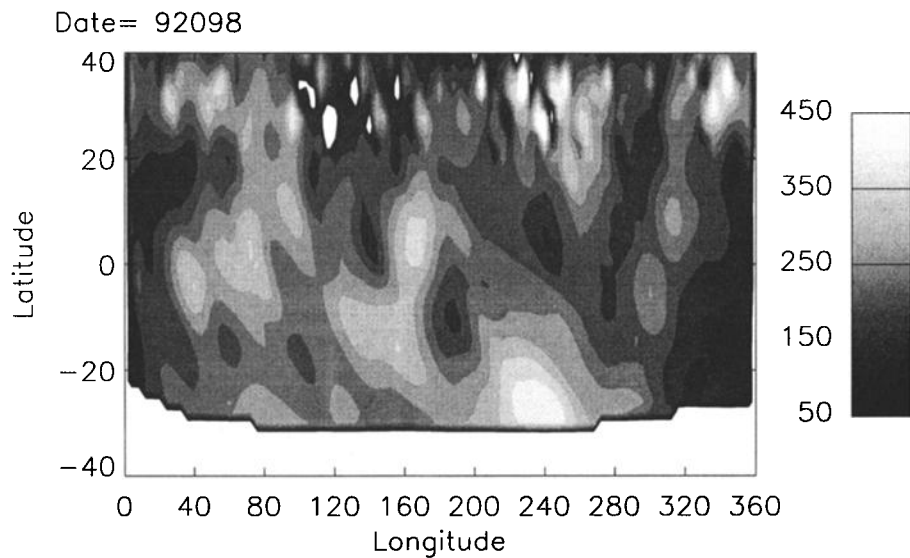


**Figure 5e.** Vertically integrated (zenithal) emission rates for the O(<sup>1</sup>S) 558-nm airglow measured by WINDII for April 7, 1992.

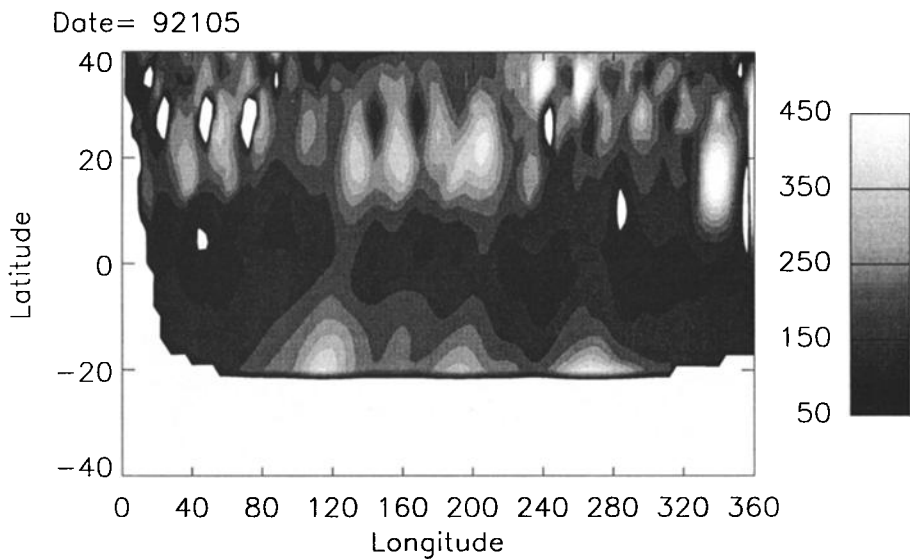


**Figure 5f.** Vertically integrated (zenithal) emission rates for the O(<sup>1</sup>S) 558-nm airglow measured by WINDII for April 14, 1992.

associated with this same feature or with the smaller depletion seen in the satellite view at 40°N and 40°E. Or perhaps these two depletions seen at the 40°N boundary of the image merge together at higher latitudes, forming a polar "hole." One cannot say from these data alone.

The sequence continues with the map for day 98 (April 7) shown in Figure 5e, in which the strong depletions have abated and the pattern has tilted so as to become more parallel to the equator. The final image in the sequence is shown in Figure 5f, for day 105 (April 14). Here the equatorial minimum has clearly reformed, while the brighter midlatitude regions are very patchy. In summary, as seen in the integrated emission rates, the global springtime transition is seen as an apparent rotation from isophotes aligned parallel to the equator to those with a primarily north-south alignment that cut across the equator and that are marked by deep depletions, with a rotation back to the parallel alignment afterwards. This is consistent with the ground-based observation of a single emission rate and temperature "pulse" over a given station.

#### 4. Wind Observations from WINDII

In Figure 6a we show the mean zonal wind determined by WINDII as a function of time, averaged for the years 1992 and 1993, and as a function of altitude, for the latitude of 40°N. In January the winds are westward from 110 km (the highest altitude of data presentation) down to about 94 km. As winter progresses toward spring, the winds reverse from westward to eastward, with the reversal date increasing with increasing

altitude. For the end of March the reversal altitude is at 107 km, implying an interaction region well above the airglow layer that suggests an association with the atomic oxygen reservoir, from which downward diffusion or mixing takes place. It is interesting to note that the eastward jet whose maximum velocity of  $40 \text{ m s}^{-1}$  occurs at 94 km in May has no counterpart in the northern autumn. For 40°S, shown in Figure 6c, the pattern is reversed with the eastward jet peaking in altitude in November. For the equator, shown in Figure 6b, there is little seasonal variation.

In summary, from January to March the northern hemisphere wind reversal (westward above and eastward below) has gradually moved up through the altitude range of observation. In Figure 7 we show the data day by day during the transition period. It must be noted that for these daily wind patterns, what is shown is the total wind. These daily winds, with the inclusion of instantaneous tidal components, represent the actual winds present over the ground stations, and thus more closely correspond with the behavior of the ground-based airglow observations. Figure 7a shows the zonal wind for March 25, 1992, as a function of latitude and altitude. As in the previous averaged data, we see westward winds at the equator through the altitudes of airglow emission, and wind reversals with altitude at midlatitudes. For the northern hemisphere the reversal is around 110 km, but the zero-wind line is tilted, so that it is at a higher altitude at higher latitudes. By March 27, shown in Figure 7b, the reversal has moved upward so that it is eastward over the whole altitude range at 35°, and the tilt of the zero-wind line has increased. For March 31, shown in Figure 7c the reversal appears complete, with lines of constant wind near vertical. This pattern continues in Figure 7d, for April 4, but with winds of increased magnitude near 40°.

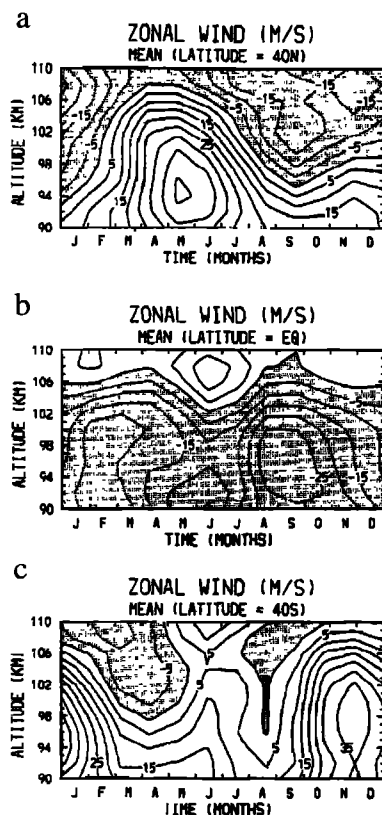


**Figure 6.** Zonal wind observed by WINDII as a function of the month of the year for three different latitude regimes, including (a) 40°N, (b) the equator, and (c) 40°S.

#### 5. Longitudinal Variations

The emission rate patterns of Figure 5 are complicated to interpret, so we present in Figure 8 simple line plots of volume emission rate at a fixed altitude versus longitude for a fixed latitude band, 42° - 45°N, for each of the six selected days during the 1992 transition period. In Figure 8a, day 92085 (March 25), we see a simple wavenumber 1 pattern varying roughly from 100 photons per  $\text{cm}^{-3} \text{ s}^{-1}$  in the valley to 250 photons per  $\text{cm}^{-3} \text{ s}^{-1}$  at the peak, and in Figure 8b for March 28 the pattern is similar. However, on March 31 (Figure 8c) the pattern has dramatically altered to a kind of square-wave, with minimum values near 50 photons per  $\text{cm}^{-3} \text{ s}^{-1}$  in the European sector and maxima reaching 500 photons per  $\text{cm}^{-3} \text{ s}^{-1}$  in the North American sector. By April 4 (Figure 8d) the contrast has weakened, and the pattern has shifted to put the minimum in the American sector and the maximum in the European sector, all of which is consistent with the ground-based data. By April 14 (Figure 8f) the regular wavenumber 1 pattern has been reestablished but with a minimum near 50 photons per  $\text{cm}^{-3} \text{ s}^{-1}$  and a maximum near 350 photons per  $\text{cm}^{-3} \text{ s}^{-1}$ . So a depleted region still exists, near 180° longitude, a region more depleted than that which existed at any longitude before the transition began. This is consistent with what is observed at the ground-based sites. For each longitude profile in Figure 8 the local time is shown. During the entire period the local time changes from 0500 to 0020 LT, and this can have some influence on the emission rates. However, during the postmidnight period the effect is not large and so does not unduly perturb the transition pattern that has been described.

Space precludes presenting the same profiles for other

latitudes, but we briefly describe what was found. At the equator the wavenumber 1 is also evident in emission rate before the transition with a very low valley value of about 20 photons per  $\text{cm}^{-3} \text{s}^{-1}$ . A planetary scale perturbation is seen during the transition, though it is not as large as that at midlatitudes, and following the springtime transition, the emission rate values are larger than they were before, near 200 photons per  $\text{cm}^{-3} \text{s}^{-1}$ . At  $40^\circ\text{S}$ , the emission rate is high before the transition occurs, about 300 photons per  $\text{cm}^{-3} \text{s}^{-1}$ . A planetary scale perturbation is seen, and after the transition is over the emission rate is lower, around 200 photons per  $\text{cm}^{-3} \text{s}^{-1}$ .

## 6. Evidence of Vertical Motion

The extremely large emission rate perturbations observed require a mechanism for this global redistribution of atomic oxygen. Ward *et al.* [1997] showed that the emission rate perturbations associated with the quasi 2-day wave were the result of vertical motions. Accordingly, the springtime transition cannot be simply a "rotation" of the global pattern but rather a dynamical perturbation which produces large-scale planetary structures in emission rate through strong vertical motions leading to localized enhancements and depletions and perhaps also to a long-term temporal depletion in atomic oxygen. Support

for this hypothesis is provided by individual profiles of WINDII emission rate, shown in Figures 9a and 9b. These profiles are for March 31, 1992 (Figure 5c), the day of the maximum at Stockholm, and they consist of six successive volume emission rate profiles taken along each of two orbit tracks four orbits apart. The first track (Figure 9a) passes through the peak values of the planetary scale "square wave" reaching values of 400 photons per  $\text{cm}^{-3} \text{s}^{-1}$  near  $310^\circ$  longitude, while the second (Figure 9b) passes through the deep minimum that reaches 50 photons per  $\text{cm}^{-3} \text{s}^{-1}$  near  $40^\circ$  longitude. The latitudes for each pair of profiles are  $30^\circ$ ,  $33^\circ$ ,  $38^\circ$ ,  $40^\circ$ ,  $41^\circ$  and  $42^\circ$ . For the first profile of Figure 9a we see for the "maximum" track a profile with a primary maximum at 93 km and a secondary maximum at 99 km; the "normal" altitude for the green line peak is 97 km. For the "minimum" track shown in Figure 9b the corresponding profile is single and coincides in altitude and peak emission rate almost exactly with the secondary 99-km peak of the maximum profile, with a peak volume emission rate of 175 photons per  $\text{cm}^{-3} \text{s}^{-1}$ . That is, at  $30^\circ$  latitude the maximum profile differs from the minimum by the addition of a second emission layer with a peak at 93 km, having a peak emission rate of 200 photons per  $\text{cm}^{-3} \text{s}^{-1}$ . In the next pair of profiles, at  $33^\circ$ , the minimum profile has hardly changed, while for the maximum profile the lower layer has strengthened to about 230 photons per  $\text{cm}^{-3} \text{s}^{-1}$  so that its double peak is barely evident.

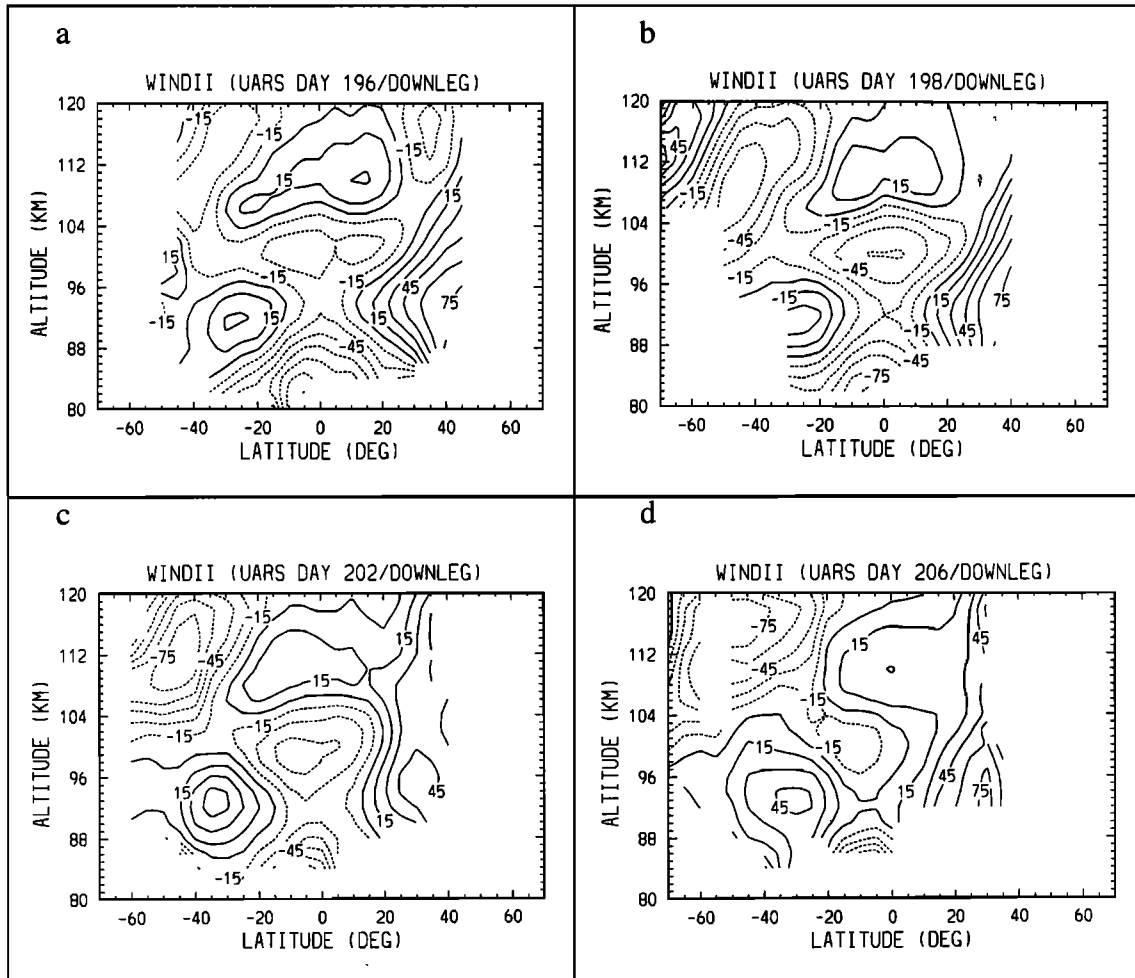


**Figure 7.** Zonal wind as a function of altitude and latitude for the 4 days of the event, including (a) day 196, (b) day 198, (c) day 202, and (d) day 206. Note the rapid steepening of the wind contours near  $40^\circ\text{N}$ .



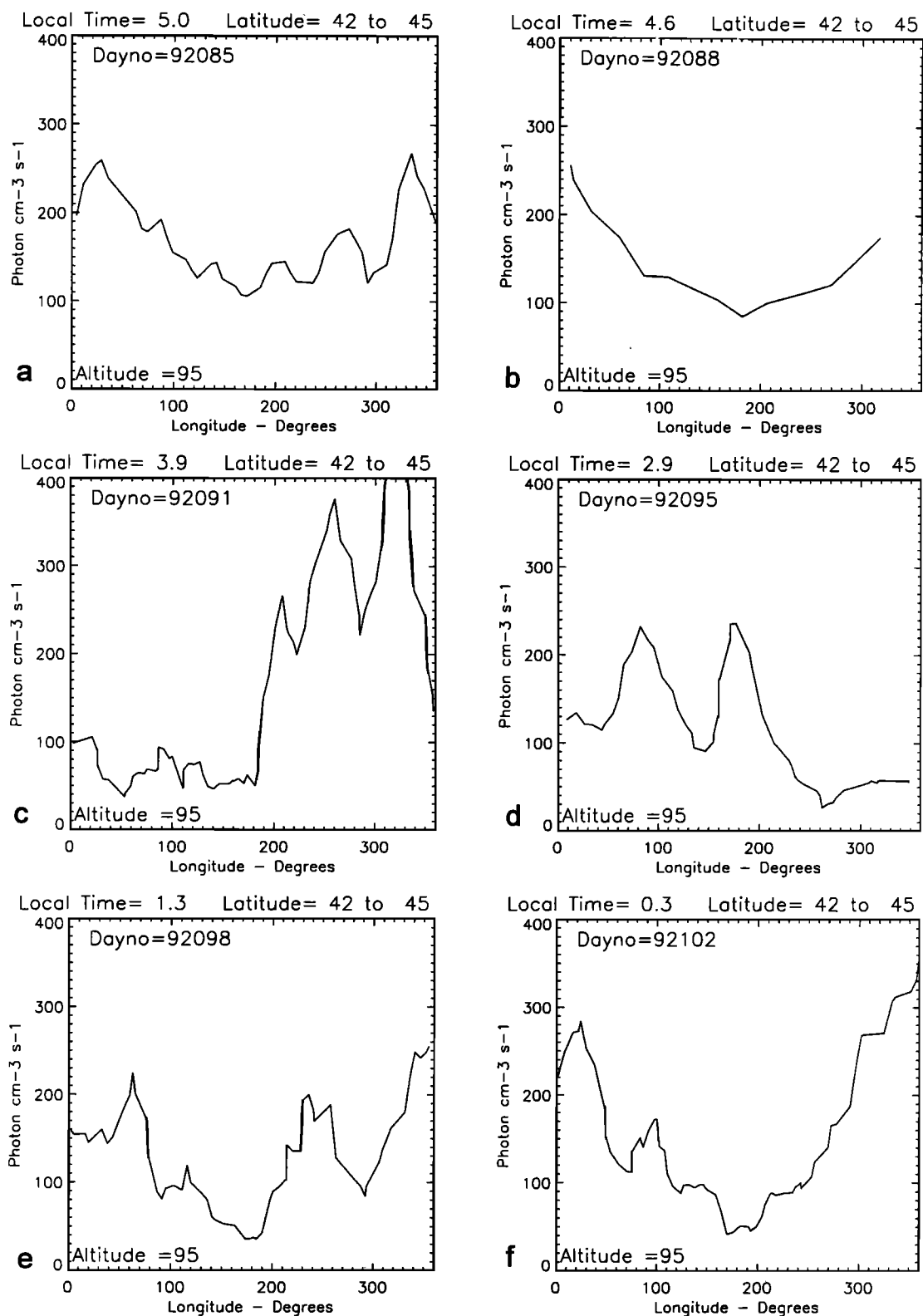


**Figure 8.** Volume emission rate (photons per  $\text{cm}^{-3} \text{s}^{-1}$ ) for the OI-558 nm emission at an altitude of 95 km plotted versus longitude for a latitude band  $40^{\circ}$ - $45^{\circ}\text{N}$  for six days during the northern springtime transition of March 25 to April 14, 1992, including (a) March 25, (b) March 28, (c) March 31, (d) April 4, (e) April 7, and (f) April 14.

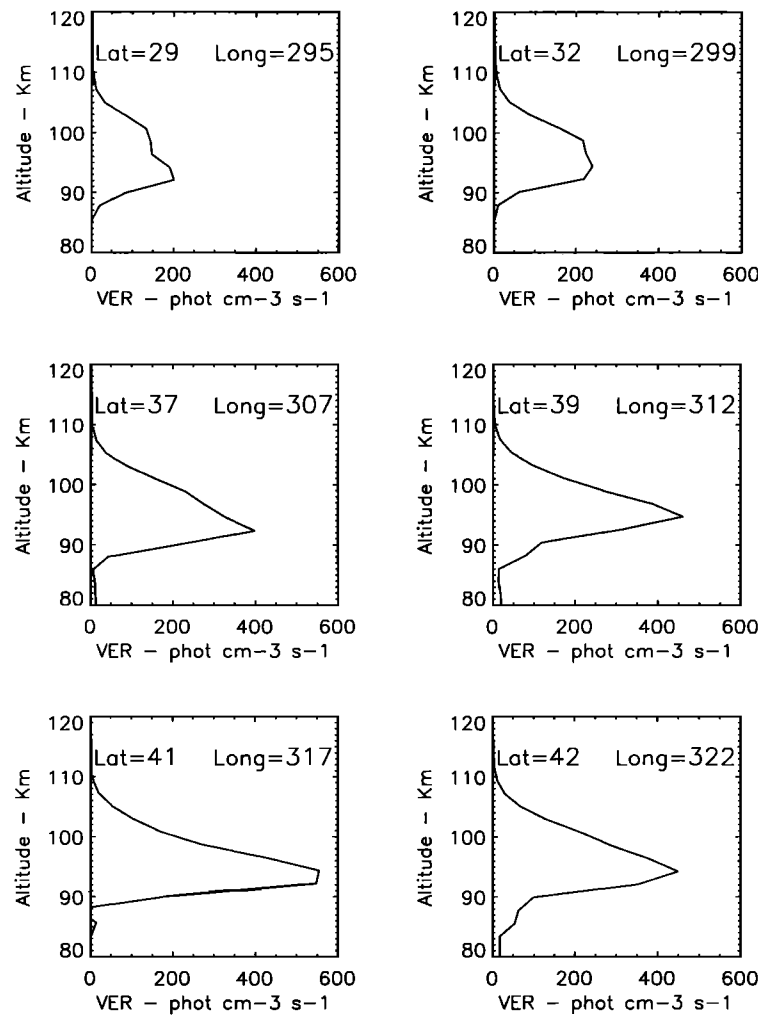


**Figure 9a.** A sequence of volume emission rate profiles taken by WINDII along the spacecraft track on March 31 near a longitude of  $300^\circ$ . The latitude, longitude, and local time for each profile are shown.

For the next profile, near  $38^\circ$ , there is a drastic change between the corresponding profiles of the two tracks. For the minimum, the peak emission rate has dropped to about 50 photons per  $\text{cm}^{-3} \text{s}^{-1}$  and become a double peak. The upper of these, at 101 km, is slightly stronger than the lower one at 95 km. For the maximum profile, the peak emission rate has almost doubled, to 400 photons per  $\text{cm}^{-3} \text{s}^{-1}$ , and the altitude of this lower level peak has lowered further from 93 to 92 km. The upper peak is just barely evident, as an inflection in the topside curve. In the next (fourth) profile, at  $40^\circ$ , the minimum profile has weakened further, and the lower peak is now stronger than the upper. The maximum profile has strengthened even more, and the next (fifth) profile has increased to about 550 photons per  $\text{cm}^{-3} \text{s}^{-1}$ , while the minimum profile has become single-peaked, a rounded curve extending to 110 km on the topside and 90 km below. From corresponding profiles that had similar peak emission rates at  $30^\circ$  latitude, the corresponding profiles at  $41^\circ$  latitude now have an emission rate ratio at the peak of 550/50, a factor of 11, a truly drastic perturbation. For the final pair of profiles the one on the minimum track is little changed, and the one on the maximum track has slightly weakened.

These data also show that the observed enhancements in emission rate occur in a layer at 92 km, well below the normal

oxygen airglow altitude of 97 km. These dramatic features of Figure 9 correspond to the behavior of the springtime transition as observed at the ground-based stations. The factor-of-eleven ratio observed by WINDII between two longitudes  $90^\circ$  apart is about the same as that seen between the peak and depletion at Bear Lake and the other stations. These perturbations in the vertical profiles confirm strong downward motions in the enhanced regions, in which air that is rich in atomic oxygen is moved into an oxygen-poor region as described for the 2-day wave by Ward *et al.* [1997]. Similarly, in the depleted regions the vertical motions must be weak, or upward. Large-scale mean vertical winds have been deduced from the WINDII data by Fauliot *et al.* [1997]; values of a few  $\text{cm s}^{-1}$  were found, in good agreement with values determined by Portnyagin *et al.* [1995] from an empirical model based on ground-based wind measurements.

## 7. Discussion

Space limitations preclude the presentation of data for years additional to those shown here, but in order to confirm the regular behavior of the springtime event, we show in Figure 10 the OI 557.7-nm emission rates from MISU and OHP for 1995. For

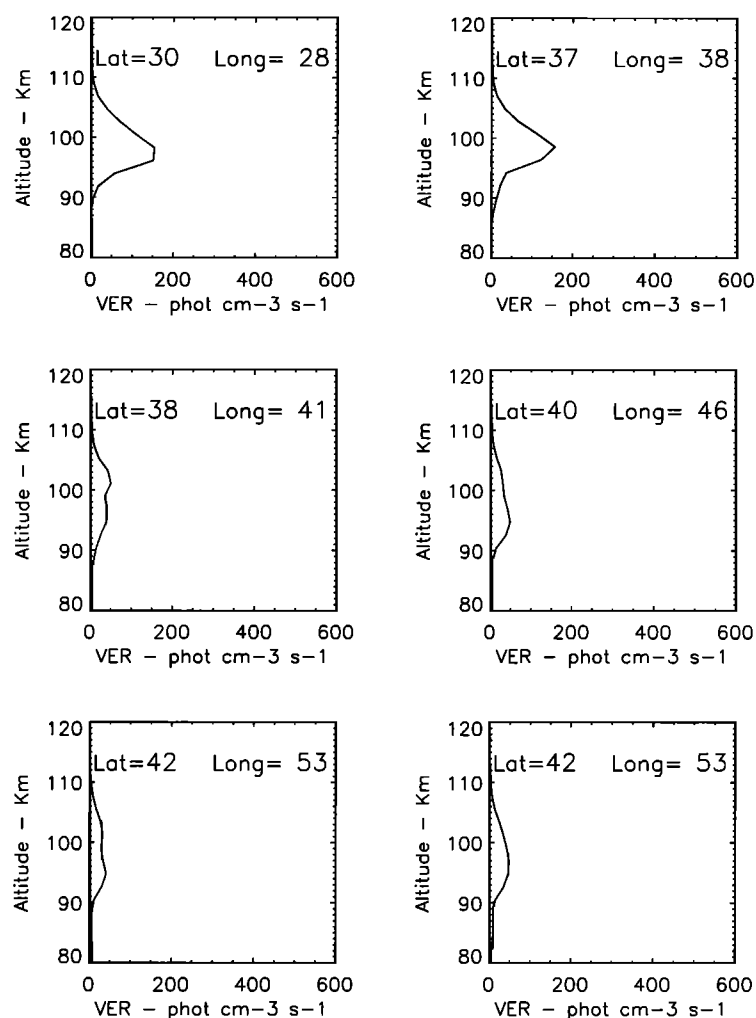


Figure 9b. Sequence of profiles as in Figure 9a, except that the longitude is near 40°.

OHP there is a pronounced peak in the emission rate on March 29, falling 4 days later to the value existing before the enhancement. At MISU the peak is 3 days later than that for OHP; four days later, it has fallen to a value somewhat below that prior to the event, and it is then followed by a number of secondary peaks. Compared with 1992-1993, the depletion level for 1995 is not as far below that prior to the peaks as it was for

the earlier years. It is remarkable that the dates of the peaks for all 3 years studied here are so similar.

The peaking of emission rate as seen on the ground appears to result from the formation of a second airglow layer near 92 km. The coherence of the emission rate and temperature perturbations as seen from the ground points to adiabatic compression relating to the downward motions already suggested as a mechanism. After the peak has passed, the temperature returns, apparently reversibly, to its normal value, but the atomic oxygen remains depleted as a result of the rapid recombination rate and the time required to replace the atomic oxygen at these altitudes. The enhanced airglow is a measure of the enhanced recombination rate, but this visible signal is only the tip of the iceberg, as it were, as many of the recombinations result in states that are quenched before radiation can occur. This indicates that the drastic rise in emission rate is associated with a total loss of atomic oxygen that is not replaced for days or even weeks. The longer duration of the depletion at MISU as compared with that at BLO very likely reflects the longer recovery time of the atomic oxygen at high latitudes. We recall that the hydroxyl emission did not show a deep minimum corresponding to the oxygen depletion. The primary excitation mechanism for the hydroxyl emission is as follows:  $O + O_2 \rightarrow O_3$ , followed by  $H + O_3 \rightarrow OH^* + O_2$ . Here  $OH^*$  denotes the upper state of the Meinel bands. From these equations it is apparent that while

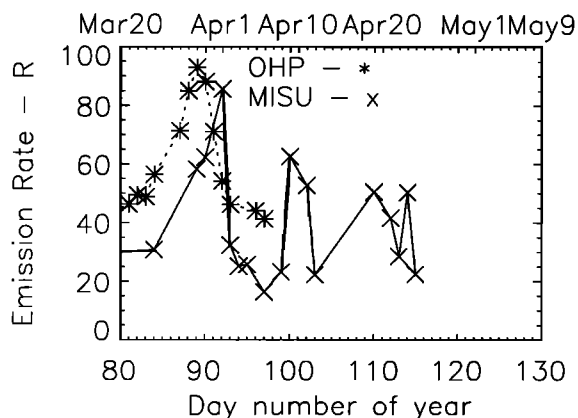


Figure 10. OI 557.7-nm emission rates at OHP and MISU for northern springtime 1995.

depleted atomic oxygen in isolation reduces the hydroxyl emission, the depletion of O is negated by another effect. The production rate of  $O_3$  is proportional to the product of the atomic and molecular oxygen concentrations, so that it is plausible that with the rapid conversion of atomic to molecular oxygen associated with the emission peak, the rate of production of ozone is little changed, allowing the hydroxyl emission to return to its prior value when the adiabatic compression has passed.

The mechanism by which the wind reversal leads to the strong vertical motions on a planetary scale deserves further investigation. Although the averaged wind data shown in Figure 6 suggests a gradual change in the wind pattern, the day-by-day wind fields of Figure 7 show a more rapid change that corresponds closely in time to the rate of change in emission rate as seen in the satellite and ground-based data. The drastic change in the background zonal circulation affects all the components of the wind system. This includes the changed contribution of the semidiurnal tide, and the reversal of the mean vertical wind from a winter-like motion (downward) to a summer-like motion (upward).

More difficult questions are how the springtime transition as described here relates to stratospheric warmings on one hand, and on the other the established equinoctial effects such as the maximum in amplitude of the diurnal tide [McLandress *et al.*, 1996], and the maximum in the mid-latitude airglow [Cogger *et al.*, 1981]. Related to this is the question of a northern hemisphere autumnal transition. While these questions remain to be investigated, the springtime transition will likely prove to be an important insight in the exploration of these semi-annual characteristics that are, as yet, poorly understood.

## 8. Conclusions

1. As observed by ground-based optical instruments, the springtime transition as observed in the northern hemisphere is characterized by the sudden rise (over a few days) in integrated emission rate for the oxygen and hydroxyl airglows by a factor of 2-3, followed by a decrease in the oxygen airglow from the peak value by a factor of 10, and a return of the hydroxyl emission to its value prior to the enhancement.

2. Airglow temperatures obtained from these emissions are coherent with the emission rates, suggesting that the enhancement is the result of adiabatic compression of the airglow layer. The temperature perturbations are large; for the  $O_2$  atmospheric band the change is from 230 to 163 K in a period of just 4 days.

3. The global integrated emission rate pattern observed by WINDII shows isophotes that are aligned parallel to the equator prior to the transition, with an equatorial minimum, and these isophotes rotate to become nearly parallel to the meridian, returning to an equatorial alignment again afterward.

4. The satellite and ground-based views are consistent in that at a ground-based site the enhancement appears as a pulse that passes a given ground station only once. Specific comparisons of the satellite and ground-based data agree well.

5. Plots of longitudinal variation show the transition pulse as a large planetary-scale feature (wavenumber 1) with extremely large peak-to-valley ratios, of about 10.

6. WINDII emission rate profiles show that these planetary scale features are accompanied by strong vertical motions; the emission rate enhancement is manifested in the formation of a second emission layer at about 92 km.

7. These strong downward motions indicate a rapid conversion of atomic to molecular oxygen, which is not immediately reversible, causing the long-term depletion following the

transition. The enhanced WINDII emission rate profiles are consistent with the enhancements of ground-based observations of the oxygen and hydroxyl airglows.

8. The WINDII wind measurements suggest that this emission rate perturbation is associated with the springtime wind reversal, in which the altitude of reversal rises gradually to some critical altitude. At the same time, the slope of the latitudinal wind gradient rapidly steepens.

9. The springtime transition as described here appears to be just part of the entire global picture of the dynamics of the semi-annual variation of the lower thermosphere, which deserves a more comprehensive investigation.

**Acknowledgments.** The WINDII project is sponsored by the Canadian Space Agency and the Centre National d'Etudes Spatiales of France and supported by the Natural Sciences and Engineering Research Council of Canada.

Janet G. Luhmann thanks David Rees and another referee for their assistance in evaluating this paper.

## References

- Cogger, L.L., R.D. Elphinstone, and J.S. Murphree, Temporal and latitudinal 5577 Å airglow variations, *Can. J. Phys.*, **59**, 1296-1307, 1981.
- Fauliot, V., G. Thuillier and F. Vial, Mean vertical wind in the mesosphere-lower thermosphere region (80 - 120 km) deduced from the WINDII observations on board UARS, *Ann. Geophys.*, **15**, 1221-1231, 1997.
- Gault, W.A., et al., Validation of  $O(^1S)$  wind measurements by WINDII: The WIND imaging interferometer on UARS, *J. Geophys. Res.*, **101**, 10,431-10,440, 1996.
- McLandress, C., G.G. Shepherd, and B.H. Solheim, Satellite observations of thermospheric tides: Results from the wind imaging interferometer on UARS, *J. Geophys. Res.*, **101**, 4093-4114, 1996.
- Portnyagin, Y. I., J.M. Forbes, T.V. Solovjeva, S. Miyahara, and C. DeLuca, Momentum and heat sources of the mesosphere and lower thermosphere regions 70 - 110 km, *J. Atmos. Terr. Phys.*, **57**, 967-977, 1995.
- Shepherd, G.G. et al., WINDII: The wind imaging interferometer on the upper atmosphere research satellite, *J. Geophys. Res.*, **98**, 10,725-10,750, 1993.
- Shepherd, G.G., C. McLandress and B.H. Solheim, Tidal influence on  $O(^1S)$  airglow emission rate distributions at the geographic equator as observed by WINDII, *Geophys. Res. Lett.*, **22**, 275-278, 1995.
- Stegman, J., D. Murtagh and G. Witt, Extremes of oxygen airglow intensity (abstract), *Eos Trans. 73(14), AGU, Spring Meeting Suppl.*, S222, 1992.
- Thuillier, G., V. Fauliot, M. Herse, L. Bourg, and G.G. Shepherd, MICADO wind measurements from Observatoire de Haute-Provence for the validation of WINDII green line data, *J. Geophys. Res.*, **101**, 10,431-10,440, 1996.
- Ward, W.E., B.H. Solheim, and G.G. Shepherd, Two day wave induced variations in the oxygen green line volume emission rate: WINDII observations, *Geophys. Res. Lett.*, **24**, 1127-1130, 1997.
- Wiens, R.H., S.P. Zhang, R.N. Peterson, and G.G. Shepherd, MORTI: A mesopause oxygen rotational temperature imager, *Planet. Space Sci.*, **39**, 1361-1375, 1991.
- Wiens, R.H., S.-P. Zhang, R.N. Peterson, and G.G. Shepherd, Tides in emission rate and temperature from the  $O_2$  nightglow over Bear Lake Observatory, *Geophys. Res. Lett.* **22**, 2637-2640, 1995.
- P. Espy, Embry-Riddle Aeronautical University, Daytona Beach, FL 32114-3900.
- C. McLandress, G. G. Shepherd, and R. H. Wiens, Centre for Research in Earth and Space Science, York University, 4700 Keele Street, Toronto, ON, Canada, M3J 1P3. (gordon@windii.yorku.ca)
- J. Stegman, Arrhenius Laboratory, Stockholm University, Stockholm, S-106 91, Sweden.
- G. Thuillier, Service d'Aéronomie, B.P. No. 3, 91371 Verrières-le-Buisson CEDEX, France.

(Received May 11, 1998; revised August 20, 1998; accepted August 21, 1998.)